communications physics

A Nature Portfolio journal

Article

https://doi.org/10.1038/s42005-026-02640-5

Rigidity control of general origami structures

Rongxuan Li & Gary P. T. Choi ✉

Origami has inspired the modern design of flexible structures in science and engineering. However, the rigidity control of general origami structures beyond the well-studied Miura-ori pattern remains unclear. Here we show that the rigidity of a wide range of origami structures can be controlled by enforcing or relaxing the planarity condition of selected facets. Through numerical simulations on origami structures with different facet selection rules, we analyze how their geometry and topology affect their degrees of freedom. We also study the probabilistic properties of the rigidity change and identify key origami structural variables that govern the critical rigidity percolation transition. Moreover, we develop a unified model that describes the relationship between the critical percolation density, facet geometry and selection rules. Altogether, our work highlights the intricate similarities and differences in the rigidity control of general origami structures, shedding light on the design of flexible mechanical metamaterials for practical applications.

Origami (paper folding) has a long history in various cultures[1] and was commonly used for ceremonial and recreational purposes. Over the past several decades, it has become increasingly popular among not just artists but also scientists and engineers, and numerous efforts have been devoted to the creation and analysis of different origami structures[2–8] as well as their applications to the design of soft robots[9,10], logic gates[11,12], and aerospace structures[13].

Miura-ori structures[14], as a prime example of origami structures with widespread applications in science and engineering, have been extensively studied. In particular, several prior works have explored their mechanical properties[15,16] and geometric design[17,18]. In a recent work[19], Chen and Mahadevan studied the stochastic control of the rigidity of Miura-ori structures. More recently, Li and Choi[20] studied the rigidity percolation transition in floppy Miura-ori structures using the idea of explosive percolation[21–23]. Besides Miura-ori structures, the rigidity of some other origami structures has also been analyzed in recent studies[24–28]. However, the rigidity control of more general origami structures remains less understood. Specifically, it is not yet known how local enforcement or relaxation of facet planarity affects rigidity across diverse origami families, whether such changes can produce abrupt rigidity transitions, or which structural features govern the transition point.

Origami structures used in practice span several broad classes with distinct geometric and topological characteristics. The three major classes commonly used in practice are shown in Fig. 1: (a) *periodic origami*, (b) *rotational origami*, and (c) *perforated origami*. In the class of *Periodic Origami* structures, the folds are formed in a periodic and scalable manner. One classical example is the Miura-ori pattern[14], which consists of identical four-coordinated quadrilateral facets. Two other examples are the Huffman Rectangular Weave pattern, consisting of triangular, rectangular, and trapezoidal facets, and the Huffman Waterbombs, consisting of triangular and square facets, both by David Huffman[29]. In the class of *Rotational Origami* structures, the creases form foldable structures with rotational symmetry. Examples include the Lang Oval (by Robert Lang), the Hex/Tri tessellation (by Kendrick Feller), and the Lang Honeycomb (by Robert Lang)[8]. For the *Perforated Origami* structures, the origami folds are designed on a perforated sheet, with examples including the Kirigami Honeycomb, the Perforated Triangle by Johann Kreuter, and the Auxetic Triangle tessellations (see also[30,31] and Supplementary Note 1 for more details). These classes differ substantially in facet shape, connectivity, and perforation, making them a useful setting for understanding how structural features influence rigidity.

The prediction of critical transitions in complex systems has long been of broad interest[32–34]. In origami structures, the critical transition density at which rigidity is gained or lost is especially relevant to applications in mechanical memory[11,35], tunable stiffness and deployable structures[36], and adaptive metamaterials[19]. Operating near this threshold enables programmable switching between floppy and rigid states, which is important for reconfigurable design and mechanical information encoding. A simple relation between the critical transition density and structural descriptors would therefore be valuable for the design and control of origami-based systems.

In this work, we combine numerical and theoretical analyses to study rigidity control in general origami structures. By enforcing or relaxing the planarity of selected facets under different facet-selection rules, we track the evolution of the degrees of freedom (DOF) and identify the critical density at

Department of Mathematics, The Chinese University of Hong Kong, Hong Kong, China. ✉e-mail: ptchoi@cuhk.edu.hk

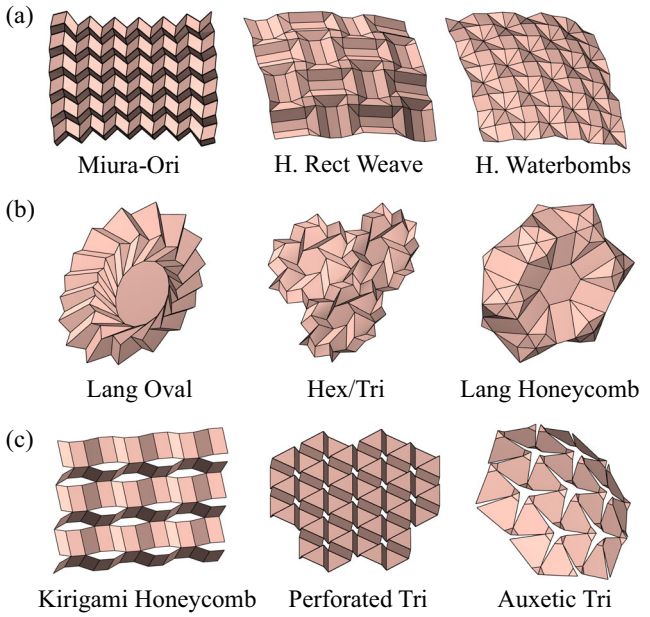

Fig. 1 | Different classes of origami structures considered in our study. a Periodic origami structures including the Miura-ori, the Huffman Rectangular Weave, and the Huffman Waterbombs. **b** Rotational origami structures including the Lang Oval, Hex/Tri, and Lang Honeycomb. **c** Perforated origami structures including the Kirigami Honeycomb, Perforated Triangle, and Auxetic Triangle.

which rigidity percolation occurs. We show that the DOF evolution and the rigidity transition are governed jointly by facet geometry, structural connectivity, the facet-selection rule, and the size of the candidate facet-selection set. We then use probabilistic model to characterize certain origami structural parameters and derive simple formulas relating the critical rigidity-percolation transition to origami structural parameters and facet-selection rules. This provides an effective framework for predicting the critical point at which rigidity is gained or lost in various origami structures. Together, these results establish a general framework for rigidity control in origami and provide design principles for programmable folded materials, deployable devices, and adaptive mechanical metamaterials. We remark that our methodology of studying rigidity percolation applies to any given origami structure, regardless of facet types or symmetry. For instance, the method can also be used for studying the rigidity percolation in the asymmetric origami structure in Fig. 2 with highly irregular facets.

Methods

As described in prior works[19,20], the Miura-ori structure is highly floppy if we allow all its quadrilateral facets to bend along the facet diagonals, while it is 1-DOF if all quadrilateral facets are enforced to be planar. Also, in between these two maximally floppy and maximally rigid states, one can enforce the planarity of certain facets sequentially based on different rules to control the rigidity transition behaviors of Miura-ori. It is natural to ask whether one can control the rigidity of more general origami structures in a similar manner and whether the transition behaviors depend on the geometry and topology of the origami structures. As demonstrated by the physical paper models in Fig. 3 (see also Supplementary Movies 1 and 2), different folding motions can be achieved by relaxing the planarity of certain facets in different origami structures. Therefore, here we consider a general origami structure and start from a maximally floppy initial state in which all of its facets are allowed to bend. We then study how the rigidity of the structure evolves from the initially floppy state to the maximally rigid state under different selection rules for enforcing the facet planarity (Fig. 4a).

Assessing the rigidity or softness

To assess the rigidity or softness of an origami structure, one has to formulate its geometrical constraints and determine the range of its infinitesimal modes of motion. Note that general origami structures may be composed of not only quadrilateral but also triangular, hexagonal, or other polygonal facets. Therefore, here we generalize the approach in refs. 19,20 to systematically formulate the *edge constraint*, *no-shear constraint*, and *facet planarity constraint* for origami structures with arbitrary polygonal facets.

Specifically, the *edge constraint* for a pair of vertices, corresponding to an edge in the origami structure, enforces that the edge length remains fixed. For each edge $(\mathbf{v}_i, \mathbf{v}_j)$, the constraint is given by

$$g_e = \| \mathbf{v}_i - \mathbf{v}_j \|^2 - l_{ij}^2 = 0, \tag{1}$$

where l_{ij} denotes the prescribed length of the edge between vertices $\mathbf{v}_i$ and $\mathbf{v}_j$.

Next, the *no-shear constraint* for every facet in the given origami structure prevents the facet from shearing. For the case of Miura-ori[19], this constraint can be enforced by simply adding a diagonal edge in every quadrilateral facet and imposing an additional edge constraint on it. In our case of general origami structures, we consider triangulating each polygonal facet and imposing edge constraints on all internal edges of the triangulation. More specifically, if we triangulate a n-sided polygonal facet $(\mathbf{v}_1, \mathbf{v}_2, \ldots, \mathbf{v}_n)$ (with $n > 3$) by introducing $n - 3$ internal edges $(\mathbf{v}_{i_1}, \mathbf{v}_{j_1}), \ldots, (\mathbf{v}_{i_{n-3}}, \mathbf{v}_{j_{n-3}})$, the no-shear constraint for this polygonal facet is then given by the edge constraints on these internal edges:

$$g_e = \| \mathbf{v}_{i_p} - \mathbf{v}_{j_p} \|^2 - l_{i_p j_p}^2 = 0, \tag{2}$$

where $p = 1, \ldots, n-3$ and $l_{i_p j_p}$ denotes the prescribed length of the internal edge between vertex $\mathbf{v}_{i_p}$ and the reference vertex $\mathbf{v}_{j_p}$. By fixing the internal edge lengths of a triangulated polygonal facet, shearing is uniformly prevented. We remark that there are many valid ways to triangulate a polygonal facet, and the specific choice of the triangulation will not affect the outcome (i.e., as long as the triangulation is valid, the shear is effectively constrained). Also, note that for a triangular facet (i.e., $n = 3$), no no-shear constraints are needed. For an origami structure containing t_{n-3} polygonal facets with n vertices, a total of $(n-3) \cdot t_{n-3}$ internal edge constraints (as no-shear constraints) are added to prevent shear. In our later computation results, we adopt a fan triangulation (all diagonals incident to one chosen vertex), consistent with Fig. 4.

We then consider the *facet planarity constraint*, which prevents a facet in the origami structure from bending. As proposed in[19], the planarity constraint of a quadrilateral facet can be imposed by enforcing the volume of the tetrahedron formed by its four vertices to be 0. More specifically, for a quadrilateral facet formed by four vertices $\mathbf{v}_1, \mathbf{v}_2, \mathbf{v}_3, \mathbf{v}_4$, the facet planarity constraint can be formulated using a scalar triple product as follows:

$$g_p = \left[(\mathbf{v}_2 - \mathbf{v}_1) \times (\mathbf{v}_4 - \mathbf{v}_1) \right] \cdot (\mathbf{v}_3 - \mathbf{v}_1) = 0. \tag{3}$$

Equivalently, the two triangles $(\mathbf{v}_1, \mathbf{v}_2, \mathbf{v}_3)$ and $(\mathbf{v}_1, \mathbf{v}_3, \mathbf{v}_4)$ will lie on the same plane. For our case of general origami structures, consider a polygonal facet with n vertices $\mathbf{v}_1, \mathbf{v}_2, \ldots, \mathbf{v}_n$. Now, note that Eq. (3) can serve as a "sub-planarity" constraint that enforces the planarity of the first four vertices $\mathbf{v}_1, \mathbf{v}_2, \mathbf{v}_3, \mathbf{v}_4$ but not necessarily the entire polygonal facet. To fully enforce the planarity of the n-sided polygonal facet, we need to introduce $n-3$ sub-planarity constraints on its $n-2$ triangulated sub-facets, such that each sub-constraint enforces the planarity of the tetrahedron formed by a pair of adjacent triangles within the polygonal facet. Together, these sub-constraints span the entire polygonal facet and ensure its overall planarity (see Fig. 4(b) for an illustration). More mathematically, we show that $n-3$ is the necessary number of constraints required to enforce the planarity for an n-sided polygonal facet.

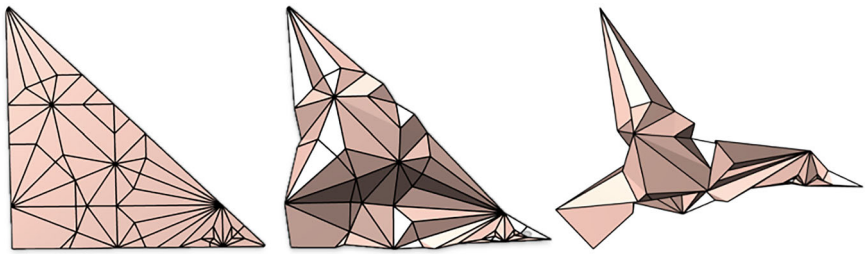

Fig. 2 | An irregular and asymmetric origami structure. Our methodology of studying rigidity percolation applies a wide range of origami structures. The simulation of such an irregular origami can be found in the Results section.

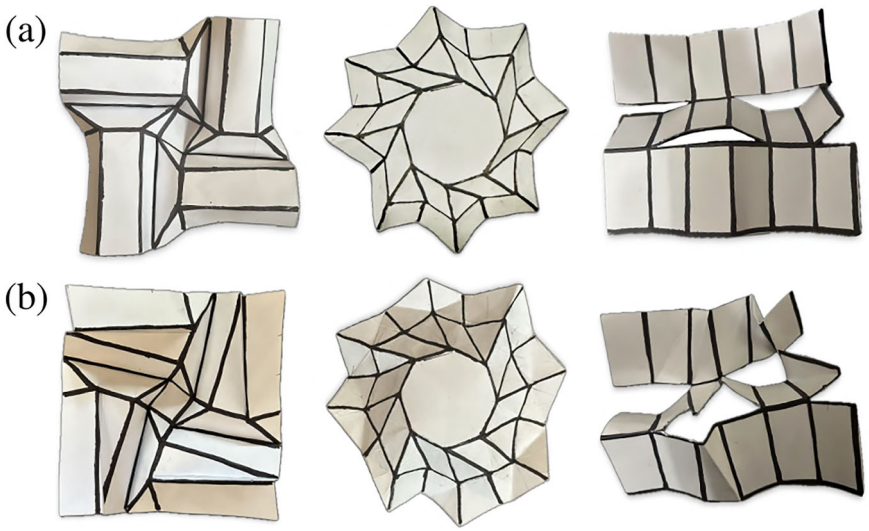

Fig. 3 | Paper-folded origami models with different folding motions. a Photographs of a folded configuration of the Huffman Rectangular Weave, Lang Oval, and Kirigami Honeycomb structures. **b** Photographs of an alternative folding motion of each structure achieved by relaxing the planarity condition of certain facets.

Theorem. The number of sub-planarity constraints required to control the planarity of an n-sided polygonal facet is exactly $n-3$.

Proof. See Supplementary Note 1, Theorem.□

We can then construct the infinitesimal rigidity matrix A as described in ref. 37 to study the possible infinitesimal modes of motion. Suppose the origami structure has E edges and V vertices. Let the structure contain polygonal facets with up to n edges. Denote N_0, N_1, N_2, …, N_{n-3} as the number of triangles, quads, pentagons, up to n-sided facets, respectively, and let the total number of facets be

$$N = N_0 + N_1 \cdots + N_{n-3}. \tag{4}$$

We impose planarity constraints on these facets, where the number of planarity constraints is M_0 for triangles, M_1 for quadrilaterals, M_2 for pentagons, and up to M_{n-3} for n-gons. The total number of planarity constraints is

$$M = M_0 + M_1 + M_2 + \cdots + M_{n-3}. \tag{5}$$

Since enforcing planarity on an n-sided facet requires $n-3$ sub-planarity constraints on its triangulated sub-facets, we define the total number of constraints on the triangulated origami as

$$K = E + \sum_{i=0}^{n-3} i \cdot (M_i + N_i), \tag{6}$$

where M_i is the number of planarity constraints for $(i+3)$-sided polygons and N_i is the number of $(i+3)$-sided polygons as described above. The infinitesimal rigidity matrix $A \in \mathbb{R}^{K \times 3V}$, constructed on the triangulated origami, encodes edge, facet, and planarity constraints. Its rank indicates the number of infinitesimal DOF of the origami structure when specific planarity conditions are imposed on polygonal facets:

$$A = \begin{pmatrix} \frac{\partial g_1}{\partial x_1} & \frac{\partial g_1}{\partial y_1} & \frac{\partial g_1}{\partial z_1} & \frac{\partial g_1}{\partial x_2} & \frac{\partial g_1}{\partial y_2} & \frac{\partial g_1}{\partial z_2} & \cdots & \frac{\partial g_1}{\partial z_V} \\ \frac{\partial g_2}{\partial x_1} & \frac{\partial g_2}{\partial y_1} & \frac{\partial g_2}{\partial z_1} & \frac{\partial g_2}{\partial x_2} & \frac{\partial g_2}{\partial y_2} & \frac{\partial g_2}{\partial z_2} & \cdots & \frac{\partial g_2}{\partial z_V} \\ \vdots & \vdots & \vdots & \vdots & \vdots & \vdots & \ddots & \vdots \\ \frac{\partial g_K}{\partial x_1} & \frac{\partial g_K}{\partial y_1} & \frac{\partial g_K}{\partial z_1} & \frac{\partial g_K}{\partial x_2} & \frac{\partial g_K}{\partial y_2} & \frac{\partial g_K}{\partial z_2} & \cdots & \frac{\partial g_K}{\partial z_V} \end{pmatrix}, \tag{7}$$

where g_1, g_2, …, g_K include all edge constraints $\{g_{e_j}\}_{i=1}^{E}$, all no-shear constraints $\{g_{n_j}\}_{j=1}^{\sum_{i=1}^{n-3} i \cdot N_i}$, all diagonal constraints, and the current set of planarity constraints on triangulated polygonal facets $\{g_{k_j}\}_{k=1}^{\sum_{i=1}^{n-3} i \cdot M_i}$, and (x_i, y_i, z_i) are the coordinates of the vertex $\mathbf{v}_i$, where $i = 1, 2, \cdots, V$.

Now, suppose there is an infinitesimal displacement $\mathbf{dv}$ added to all vertex coordinates $\mathbf{v} = [x_1, y_1, z_1, x_2, y_2, z_2, \ldots, x_V, y_V, z_V]^T$. The condition for infinitesimal rigidity is given by

$$A\,\mathbf{dv} = 0. \tag{8}$$

Thus, the infinitesimal degrees of freedom (DOF) of the origami structure correspond to the dimension of the null space of A. For V vertices, there are in total $3V$ coordinates. Removing the six trivial global rigid motions (three translations and three rotations), the DOF is given by

$$d = 3V - \text{rank}\,(A) - 6. \tag{9}$$

The infinitesimal rigidity matrix A for the initial maximally floppy structure includes only the E edge constraints and the $\sum_{i=0}^{n-3} i \cdot N_i$ no-shear

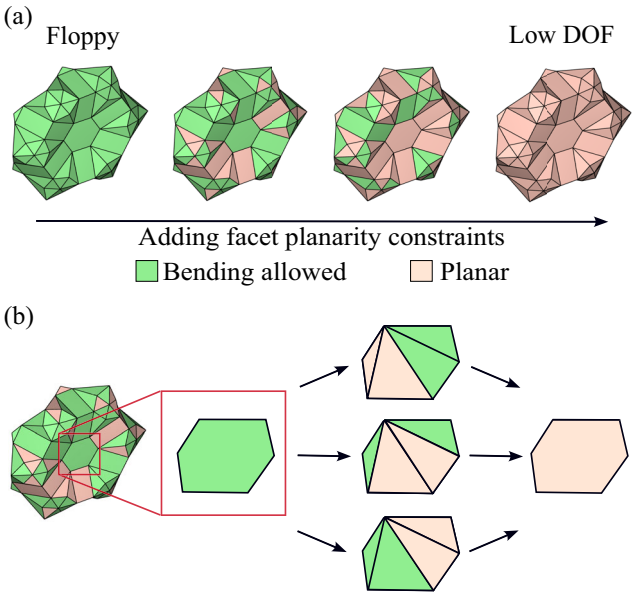

Fig. 4 | An illustration of the rigidity control process. a Starting from a maximally floppy state of a given origami structure, we consider adding facet planarity constraints based on different selection rules, thereby controlling the rigidity of the structure. **b** To enforce the planarity of a general n-sided polygonal facet, we first triangulate it by considering $n-3$ diagonal edges. Then, by enforcing the planarity for every tetrahedron formed by a pair of triangles in the polygonal facet, we can ensure the planarity of the entire facet.

constraints (i.e., $M=0$). Since $\mathrm{rank}(A_{\mathrm{initial}})$ is at most the number of its rows, the general lower bound of the DOF of the initial structure is given by

$$d_{\mathrm{initial}} \geq 3V - E - \sum_{i=0}^{n-3} i \cdot N_i - 6. \tag{10}$$

The final DOF, denoted d_{final}, depends on the geometry and topology of the origami structure and is non-negative.

Rigidity control and the DOF evolution

We then study the evolution of DOF from d_{initial} to d_{final} as planarity constraints are gradually imposed. More specifically, at each step, we select a new facet, either a triangular facet or a polygonal facet, and explicitly impose its corresponding planarity constraint. Note that the number of planarity constraints depends on the type of polygonal facet selected. If a triangular facet is selected, no planarity constraint needs to be enforced. For a general polygon with n vertices, $n-3$ planarity constraints will be imposed if the polygon is selected. We can then define the *planarity constraint density*$\rho \in [0, 1]$ as

$$\rho = \frac{\text{Number of facets selected}}{\text{Total number of facets}}, \tag{11}$$

and study how the DOF changes as the density ρ increases from 0 to 1.

Moreover, we can follow the idea of explosive percolation[21,38] and consider multiple candidate facets at each step and select one among them based on certain selection rules to control the rigidity percolation transition. Let $k \geq 1$ be a positive integer. At each step, we sample k facets randomly from the set of all available facets that have not been selected. We then select one among them based on one of the following selection rules:

- *Most Efficient selection rule*: Given k randomly sampled candidate facets $f_1, f_2, \ldots, f_k$, we temporarily add the facet planarity constraint of each f_i to the current rigidity matrix A to form A_i and compute the resulting DOF d_i. Among all k candidate facets, we select the facet that gives the minimum DOF, i.e., the facet f_c with $c = \mathrm{argmin}_i d_i$. If multiple candidates give the minimum DOF, one is selected randomly.
- *Least Efficient selection rule*: Analogous to the above rule, for each candidate facet f_i, we construct the augmented matrix A_i and compute the DOF d_i. We then select the facet that gives the maximum DOF, i.e., f_c with $c = \arg\max_i d_i$. If multiple facets give the maximum DOF, we select one among them randomly.

We can then study the effect of the power-of-choices strategy for rigidity control in general origami structures with different geometric and topological properties. Before presenting these results, we clarify that our reported DOFs are not biased by the particular triangulation choice. The triangulation is introduced to encode the no-shear condition via internal edge-length constraints, such length constraints as shown in Proposition 1 are insensitive to infinitesimal out-of-plane bending of flat facets. When planarity is enforced on a facet, the resulting sub-facet coplanarity constraints restrict the facet to the same coplanar admissible motion space under any valid triangulation. Thus, different valid triangulations mainly lead to different but equivalent linear representations of the same rigid-facet motion constraint.

Proposition 1. Edge constraints and no shear induced by triangulation can not prevent infinitesimal bending on flat facets.

Proof. In infinitesimal bending, the movement of the node is perpendicular to the plane, and the length of the diagonal edge is preserved. See Proposition Supplementary Note 1.1, for a detailed argument and proof.□

Hypergeometric model

To quantitatively study the relationship between origami geometry and selection rules with the rigidity percolation (critical transition density) of different origami structures, we need to consider both the selection parameters (i.e., the selection rule and the number of choices k) and the structural properties of the origami. To identify structural properties that govern the evolution of DOF, here we estimate and bound the theoretical probabilities of the DOF remaining unchanged or decreasing at a given density ρ using a hypergeometric model. In this model, the triangular facet ratio serves as a key parameter, highlighting it as a fundamental structural property that directly influences the evolution of DOF.

Now, denote the triangular facet ratio at constraint density ρ by $t(\rho)$, and let $N(\rho)$ be the total number of available facets for selection. Then, the number of triangular facets is given by $T(\rho) = t(\rho)N(\rho)$. Let $X(\rho)$ be the random variable representing the number of triangular facets among the k candidate facets selected at density ρ. The distribution of $X(\rho)$ follows a hypergeometric distribution:

$$P(X(\rho)=n) = \frac{\binom{T(\rho)}{n}\binom{N(\rho)-T(\rho)}{k-n}}{\binom{N(\rho)}{k}}. \tag{12}$$

Now, we denote $P_0(\rho)$ as the probability that the number of DOFs remains unchanged when the constraint density increases by one unit step, i.e.,

$$P_0(\rho) = \mathbb{P}\left(d(\rho) = d\left(\rho + \frac{1}{(\text{total \# of facets})}\right)\right), \tag{13}$$

and denote $P_1(\rho)$ as the probability that the number of DOFs decreases, i.e.,

$$P_1(\rho) = \mathbb{P}\left(d(\rho) > d\left(\rho + \frac{1}{(\text{total \# of facets})}\right)\right). \tag{14}$$

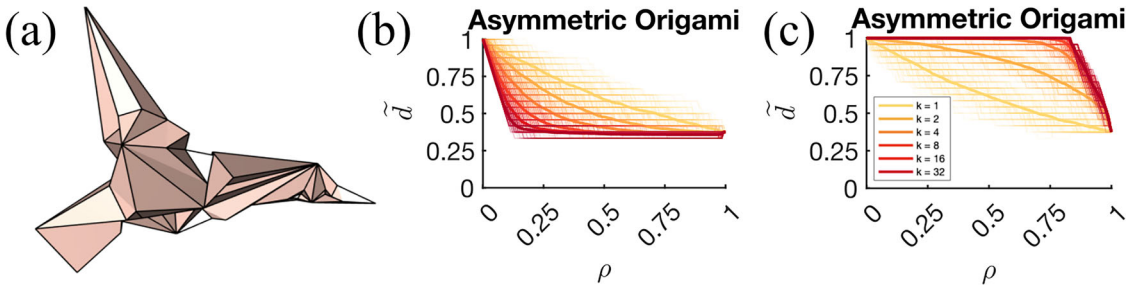

Fig. 5 | An asymmetric origami structure and the change of its normalized DOF under different rules. a An asymmetric origami structure. **b** The change in the normalized DOF under the Most Efficient selection rule. **c** The change in the normalized DOF under the Least Efficient selection rule. Here, $\tilde{d} = (d-1)/(d_{\text{initial}}-1)$ denotes the normalized degree of freedom (DOF), ρ = (Number of facets selected)/(Total number of facets) denotes the fraction of selected facets, and k denotes the number of available facets randomly sampled at each step.

Notice that under the Least Efficient selection rule, a sufficient condition for the DOF d to stay the same at ρ is that at least one triangular facet is included among the k candidates at the selection at ρ. In this case, it is guaranteed that a facet can be selected without causing a decrease in DOF by the rule. However, this condition is not necessary for the DOF to remain unchanged, as even when no triangular facet is present in the k candidates, some non-triangular redundant facets may exist among the candidates, resulting in d unchanged after the selection.

Now, note that the probability $P_0(\rho)$ that the DOF remains unchanged can be bounded below by the probability that at least one triangular facet exists among the k candidates,

$$P_0(\rho) \geq 1 - P(X(\rho) = 0) \approx 1 - (1 - t(\rho))^k. \tag{15}$$

The approximation of the hypergeometric distribution holds when $N \gg k$. Since the DOF is non-increasing throughout the process, we have the total probability split as $P_1(\rho) + P_0(\rho) = 1$, where $P_1(\rho)$ denotes the probability that the DOF decreases. Therefore, we obtain,

$$P_1(\rho) \leq P(X(\rho) = 0) \approx (1 - t(\rho))^k. \tag{16}$$

Notice that under the Most Efficient selection rule, a sufficient condition for the DOF d to remain unchanged is that all k selected facets are triangular. However, this condition is not necessary, as even if some non-triangular facets are included in the candidates, they may still be redundant with respect to the previously selected facets and thus may not lead to a DOF decrease after employing the rule.

In this case, the probability $P_0(\rho)$ that the DOF remains unchanged can be bounded below by the probability that all k candidates are triangular facets,

$$P_0(\rho) \geq P(X(\rho) = k) \approx t(\rho)^k. \tag{17}$$

Similarly, we obtain,

$$P_1(\rho) \leq 1 - P(X(\rho) = k) \approx 1 - t(\rho)^k. \tag{18}$$

The above inequalities indicate that the change in DOF at constraint density ρ is governed by the number of choices k and the triangular facet ratio $t(\rho)$.

Note that the behavior of the triangular facet ratio $t(\rho)$ is influenced by the initial triangular facet ratio $t = t(0)$, the selection rule r, and the number of choices k. To isolate structural effects, we record the initial triangular facet ratio $t = t(0)$, which serves as a structural property of the origami and depends solely on the origami type and its resolution. For each origami structure, we record the initial triangular facet ratio t, the selection rule r, and then perform numerical simulations as described in the following section.

Results

To study how the selection rules and the number of choices k affect the rigidity control of general origami structures, we performed numerical simulations in MATLAB with the Parallel Computing Toolbox used. The infinitesimal rigidity matrix A was constructed in sparse matrix format. For the DOF calculation, we followed the approach in ref. 39, using the built-in column approximate minimum degree permutation function `colamd` and the `qr` decomposition to compute the QR factorization of A. The rank of A was then approximated by counting the number of non-zero diagonal entries in the resulting upper triangular matrix R. Since the rank approximation of large matrices may be affected by numerical errors, and since all origami structures considered in our work are foldable, we further restrict the computed DOF values to lie within the feasible range $[1, d_{\text{initial}}]$. To account for floating-point errors in rank detection, we classify non-zero pivots using an adaptive threshold: `tol` = (problem size) × (machine precision) × (matrix scale), then estimate the rank by counting such pivots. See Supplementary Note 2 for a comprehensive numerical error analysis. Also, note that the construction of the rigidity matrix involves the coordinates of the vertices. In our experiments, we considered all types of origami structures in Fig. 1 at a folded configuration with a folding percentage of 25% generated using the method from[31]. In Supplementary Note 1, we further compare the simulation results with different folding percentages and show that our analyses also hold for other folding percentages.

For each type of origami structure, each choice of $k = 1, 2, 4, 8, 16, 32$, and each selection rule, we performed 100 independent simulations. In each simulation, we start from the maximally floppy state ($\rho = 0$) and select facets based on selection rules until reaching the maximally rigid state ($\rho = 1$). To facilitate comparison across different origami structures, we also consider the normalized DOF $\tilde{d}$ defined by

$$\tilde{d} = \frac{d-1}{d_{\text{initial}} - 1}. \tag{19}$$

Here, we remark that the final DOF of different structures d_{final} may vary and is not always equal to 1. Nevertheless, we normalize the DOF using $d_{\text{initial}} - 1$, instead of $d_{\text{initial}} - d_{\text{final}}$, to allow a more consistent comparison, particularly with Miura-ori. This normalization also helps us observe whether a structure tends toward a single-DOF mechanism or maintains multiple DOFs when all planarity constraints are enforced. To better illustrate these results and demonstrate that our methodology is robust across different structures, especially irregular origami, we present the simulation result of an asymmetric origami in Fig. 5. Figure 5(a) shows the asymmetric origami structure. Figure 5(b,c) plots the normalized DOF $\tilde{d}$ trajectory as the selection density ρ increases from the maximally floppy state ($\rho = 0$) to the maximally rigid state ($\rho = 1$) by iteratively selecting facets according to each rule while different colors correspond to different choice number k. For each rule and color, the faint (cloudy) curves show individual trajectories from 100 independent simulations, and the solid curve shows the corresponding mean under the color's corresponding choice number.

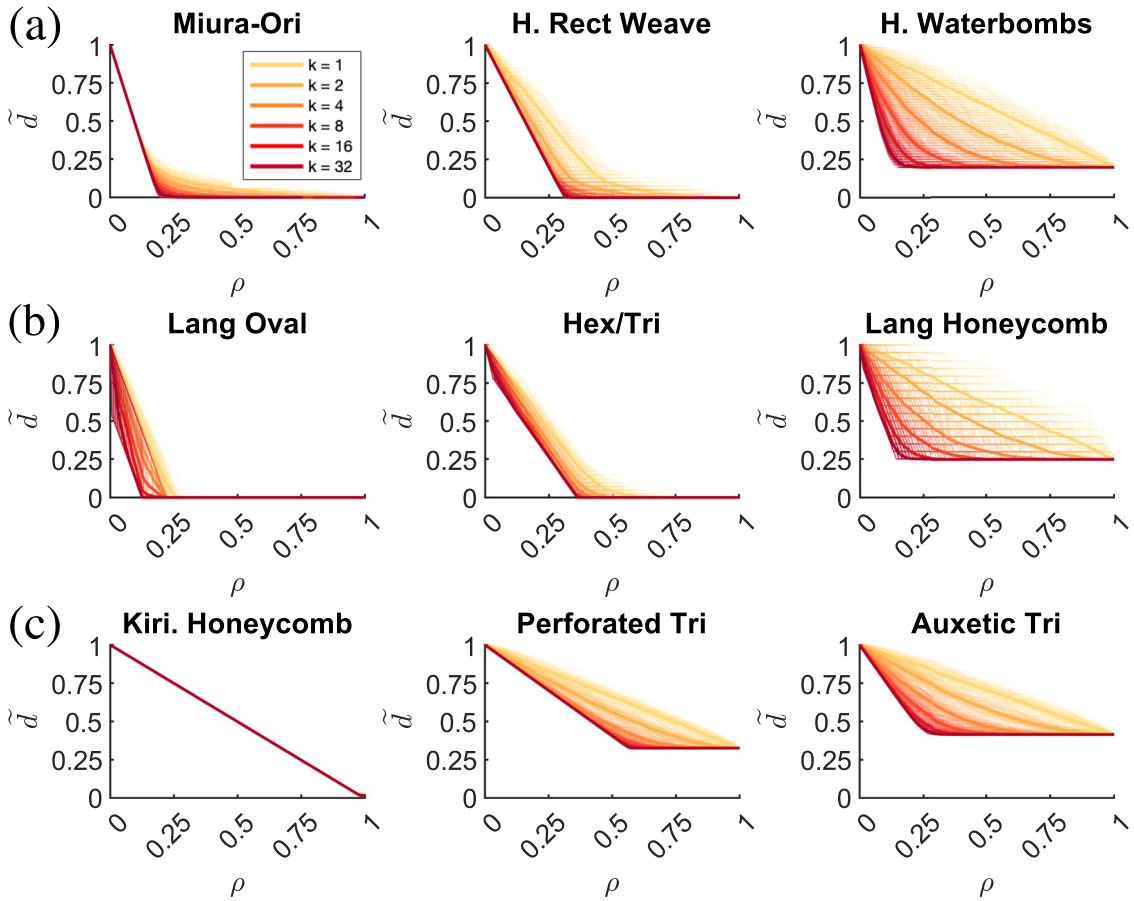

Fig. 6 | Change in the normalized DOF under the Most Efficient selection rule with different numbers of choices for nine types of origami structures. Rows (**a**)–(**c**) correspond to the Periodic Origami, Rotational Origami, and Perforated Origami structures, respectively. Within each row, the ratio of triangular facets increases from left to right across the structures. Here, $\tilde{d} = (d-1)/(d_{\text{initial}}-1)$ denotes the normalized degree of freedom (DOF), ρ = (Number of facets selected)/(Total number of facets) denotes the fraction of selected facets, and k denotes the number of available facets randomly sampled at each step. For each structure and each color, the faint curves show individual trajectories from 100 independent simulations, and the solid curve shows the corresponding mean for that choice number.

The Most Efficient selection rule

In Fig. 6, we plot the values of $\tilde{d}$ from 100 simulations under the Most Efficient selection rule across different values of k for the 9 origami patterns. The lighter transparent curves represent individual results from each of the 100 simulations for the corresponding k values, while the darker smooth curves show the mean over the 100 simulations for each setup (see Supplementary Note 3, Figs. S6–S11) for more plots with different pattern sizes).

While the Miura-ori structure exhibits a well-defined two-phase evolution of the normalized DOF $\tilde{d}$, characterized by an initial linear decrease followed by a sharp transition to a sublinear regime across all values of k[19,20] (see the uniformly linear decline for all k in the Miura-ori results in Fig. 6), general origami structures show more diverse behaviors. In particular, structures with a high proportion of triangular facets, such as the Huffman Waterbombs, Auxetic Triangle, and Lang Honeycomb, often deviate from this linear trend when k is small (see the yellow regions of the corresponding structures where the DOF shows a scattered decline in Fig. 6). This difference arises because imposing planarity on triangular facets does not reduce the global DOF, especially during early stages when such facets are inevitably selected from the small k-candidate pool. As a result, the early-stage linear decrease observed in Miura-ori becomes less consistent or even absent in these more complex patterns at small k. These observations highlight the role of structural heterogeneity and facet geometry in shaping the rigidity percolation process in general origami systems.

Nevertheless, the power of the Most Efficient selection rule, along with larger values of k-candidate pool, helps avoid the selection of triangular facets in the early stages, thereby restoring the linear regime even in individual simulations (see the red regions in Fig. 6 where a linear decrease is observed across general structures and where the linearity becomes more pronounced as k increases). The candidate sampling mechanism under high k offers a larger pool of candidate facets, thereby increasing the probability of selecting facets with more vertices at the early stage. Imposing planarity on these facets is more effective in reducing the degrees of freedom, as it constrains more vertex motions and indirectly influences adjacent facets. As a result, at larger k, a linear early-stage decrease in DOF followed by a flatter region similar to the Miura-ori is observed.

Since imposing a planarity constraint on a facet with more vertices tends to reduce the DOF more significantly, the facet type plays a crucial role in the evolution of DOF. In periodic origami structures, due to their inherent periodicity and foldability, the patterns are typically composed of quadrilaterals and triangles. This simple facet composition leads to two distinct behaviors: selecting a quadrilateral facet in the early stage decreases the DOF by one (as it contributes a single constraint row to the rigidity matrix A, as discussed in the previous section), while selecting a triangular facet does not reduce the DOF. As a result, under the Most Efficient selection rule with large k, the system tends to prioritize quadrilateral facets, leading to a linear decrease in DOF until the final value is reached, after which the curve flattens (see the first-row plots of Fig. 6).

In rotational origami patterns, central or sub-central facets with many edges and vertices are often present to achieve central rotational symmetry. For example, the Lang Oval pattern features a 17-gon, Hex/Tri features a

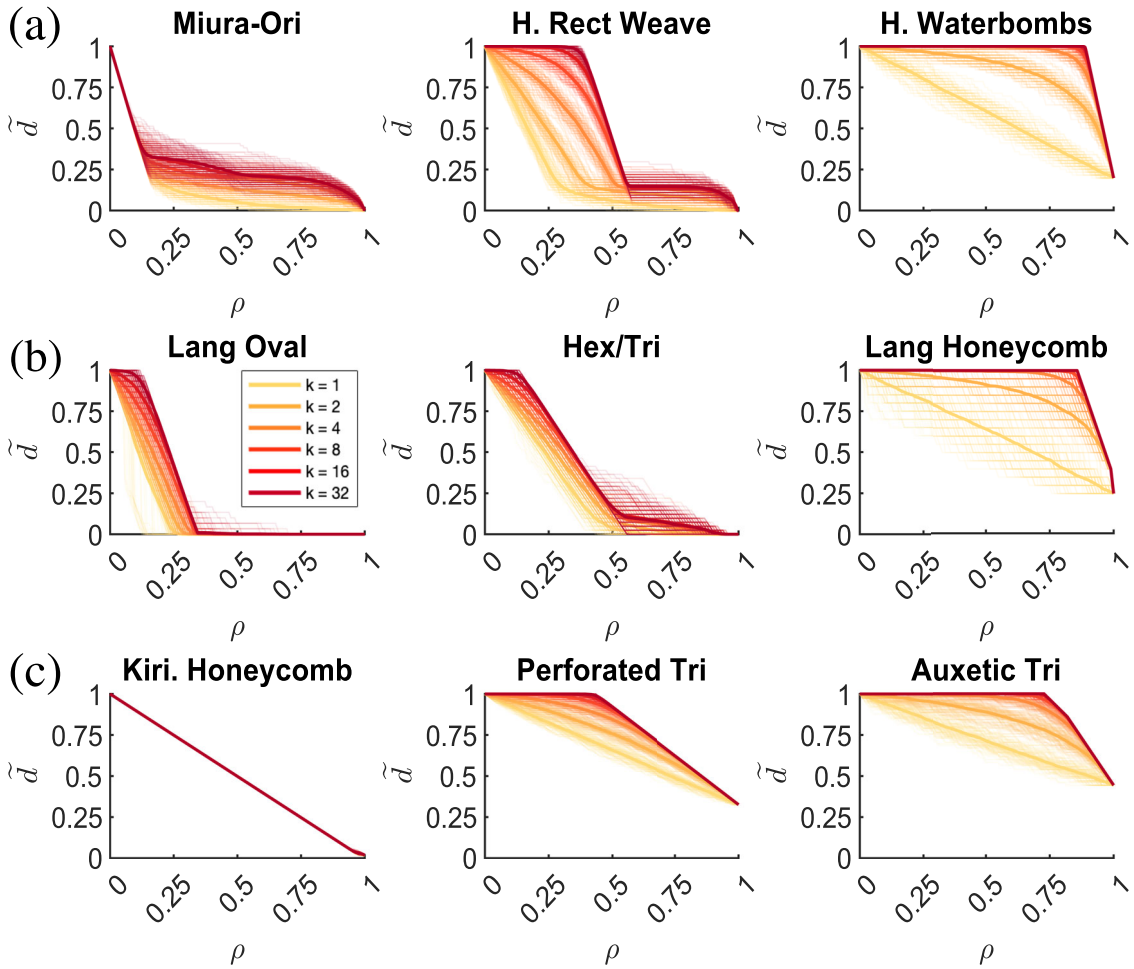

Fig. 7 | Change in the normalized DOF under the Least Efficient selection rule with different numbers of choices for nine types of origami structures. Rows (**a**)–(**c**) correspond to the Periodic Origami, Rotational Origami, and Perforated Origami structures, respectively. Within each row, the ratio of triangular facets increases from left to right across the structures. Here, $\widetilde{d} = (d-1)/(d_{\text{initial}}-1)$ denotes the normalized degree of freedom (DOF), ρ = (Number of facets selected)/(Total number of facets) denotes the fraction of selected facets, and k denotes the number of available facets randomly sampled at each step. For each structure and each color, the faint curves show individual trajectories from 100 independent simulations, and the solid curve shows the corresponding mean for that choice number.

hexagonal sub-center, and Lang Honeycomb features a central hexagon. To achieve rotational symmetry, these patterns incorporate a mix of triangular, quadrilateral, and other polygonal facets, resulting in more than two types of facets in the structure. Therefore, under the Most Efficient selection rule, combined with the power of choices, the selection process tends to prioritize hexagonal facets over quadrilaterals and quadrilaterals over triangles. As a result, the DOF evolution of rotational origami with a larger k often exhibits a piecewise linear trend, with an initial steep linear decay, followed by a slower linear regime, and finally transitioning into a nonlinear region as the remaining unconstrained facets (mainly triangular facets) will hardly affect the DOF decrease (see the second-row plots of Fig. 6).

In perforated origami structures, due to the presence of cuts between facets, the individual facet planarity is less related to each other. As a result, imposing a planarity constraint on one facet does not significantly affect the planarity of others, compared to connected origami structures. Hence, the DOF decays linearly as non-triangular facets are increasingly prioritized with larger values of k. Once only triangular facets remain, the DOF curve flattens as it reaches the final DOF value (see the third-row plots of Fig. 6). In the Kirigami Honeycomb structure, all simulation results for different values of k overlap as a linear line in the plot. This is because the structure is highly floppy and contains no linearity-breaking triangular facets, and enforcing planarity on one facet does not implicitly affect the planarity of neighboring facets at any level, due to the frequent presence of cuts between them. As a result, the DOF decreases linearly throughout the process until the end.

To obtain a more comparative conclusion, we observe that the DOF trajectories across different patterns generally exhibit a piecewise-linear decrease. In the early stage, because our selection rule prioritizes high-edge polygons, the algorithm repeatedly selects constraints associated with polygons with a similar large edge count. Moreover, these newly added constraints are often approximately independent, so the rank of the rigidity matrix increases by an almost constant amount at each step and therefore causes an almost constant DOF reduction. In the later stage, the trajectories enter a more gradual, approximately flat regime as redundancy becomes more frequent. Additionally, in this linear regime, for a relatively large k, the DOF tends to decrease more slowly as the ratio of triangular facets increases across different patterns. Finally, the standard deviation across simulations decreases as k increases, indicating that the power of choices has a strong effect, leading to a narrower transition width in rigidity percolation. This effect is particularly significant for patterns with a higher proportion of triangular facets, where the selection rule becomes more influential in avoiding the early selection of facets that do not reduce the structure's overall DOF.

The Least Efficient selection rule

Similar to the Most Efficient selection rule, Fig. 7 shows $\widetilde{d}$ from 100 simulations under the Least Efficient selection rule across different k values for all

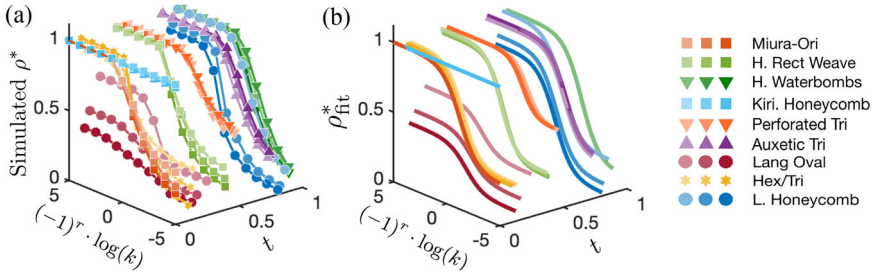

Fig. 8 | The critical transition density for the nine different types of origami structures under different selection rules and different numbers of choices *k*. Here, ρ^* denotes the critical transition density, k denotes the number of available facets randomly sampled at each step, and t denotes the triangular-facet ratio of the origami structure. The nine different types of origami structures are represented by different marker styles and colors. For a given marker symbol, different color intensities represent different resolutions of the same origami structure: a darker color indicates a larger number of facets, while a lighter color indicates a smaller number of facets. **a** The critical transition density ρ^* obtained from our simulations. **b** The fitted ρ^* obtained using the proposed model in Eq. (21). The corresponding quantitative values are provided in Supplementary Note 4.

nine types of origami patterns. The light lines indicate the individual 100 simulations. The dark lines indicate the average of the 100 simulations (see Supplementary Note 3. Figures S12–S17 for more plots with different pattern sizes).

It is easy to see that the DOF evolution of general origami structures at the early stage behaves quite differently compared to Miura-ori under the Least Efficient selection rule. Due to the presence of triangular facets, in individual simulations, the rule often selects triangular or small-vertex facets at the early stage, introducing nonlinearity in the DOF decay in the individual simulations. With a larger k, the increased sampling pool gives a better chance to select triangular facets in the early stage, which further slows down the DOF reduction. Unlike Miura-ori and Kirigami Honeycomb, which consist only of quadrilateral facets and exhibit inevitable linear DOF decay at early stages under any rule, structures with triangular facets can delay DOF reduction in the early stage. Under the Least Efficient selection rule with large k, a slower or even flat DOF transition in the early stage can be observed (see the red regions of the corresponding structures in Fig. 7, where the DOF remains flat during the early stage).

In structures where the final DOF is one, such as Huffman Rectangular Weave and Hex/Tri, the DOF trajectory then resembles that of Miura-ori, showing an initial linear decay followed by a nonlinear regime. This can be seen from the DOF evolution of the corresponding structures in Fig. 7, where the DOF remains flat at the early stage, then decreases linearly, and is eventually followed by a nonlinear region. The middle decreasing and final nonlinear regions resemble the DOF trend observed in Miura-Ori, starting from its initial linear regime. Since the triangular facets have already been selected, the algorithm inevitably begins selecting non-triangular facets, leading to further DOF reduction. Once a sufficient number of polygonal facets are selected, the Least Efficient selection rule begins to preferentially select "redundant" facets for which the planarity constraints no longer impact the DOF.

For patterns that retain multiple degrees of freedom at the final stage, the structure often contains a large proportion of triangular facets or cuts, or is composed of groups of polygonal facets that include a mix of triangular, quadrilateral, and hexagonal facets. Since the constraint selection process under the Least Efficient selection rule initially targets facets whose planarity constraints have minimal effect on the global DOF, those with fewer vertices are thus more likely to be selected in the early stage, resulting in an initial flat region. As the process progresses, it inevitably shifts toward larger or more connected facets, which constrain more degrees of freedom and lead to a more rapid reduction in DOF. As a result, in the Auxetic Triangle, Perforated Triangle, and Lang Honeycomb patterns, the DOF tends to decrease directly to the final DOF after initial flatness. This can be observed in the DOF evolution of the corresponding structures in Fig. 7, where the DOF remains flat at the early stage, then decreases linearly to the final DOF, or is followed by a steeper linear decrease leading to the final DOF. By contrast, the Kirigami Honeycomb structure is highly floppy. As explained earlier, under both rules, enforcing planarity on one facet does not implicitly constrain other facets due to the presence of cuts, resulting in no redundant constraints. Under the Least Efficient selection rule, the DOF still decreases linearly throughout the process until the end.

In conclusion, for patterns with triangular facets and relatively large k, the DOF curve typically begins with a flat regime, which can not be observed in Miura-ori due to its purely quadrilateral configuration. Then the DOF evolution enters a (piecewise) linear regime, where the number of linear segments depends on the diversity of polygon types in the origami structure. This behavior arises because the selection rule inevitably keeps choosing similar multi-edge facets over many consecutive steps, which leads to an almost constant per-step rank increase and hence an almost constant DOF reduction. Finally, A redundant nonlinear regime may or may not appear, depending on the specific geometry and connectivity of the pattern, and whether it leads to a single-DOF structure when all planarity constraints are imposed.

A unified model for the rigidity percolation transition

To study the rigidity percolation transition in different origami structures, we consider the probability of getting a minimum-DOF structure (i.e., a structure achieving the minimum possible DOF d_{final}) for each planarity constraint density ρ, defined as

$$P(\rho) = \frac{\text{Number of minimum} - \text{DOF structures at } \rho}{\text{Total number of simulations}}. \quad (20)$$

To quantify how the change in the number of choices k affects the rigidity percolation transition in different patterns and sizes, we define the *critical transition density* ρ^* as the minimum ρ with the probability of getting a minimum-DOF structure $P \geq 1/2$ in our simulations (see Supplementary Note 3, Figs. S9–S11, S15–S17 for plots of P vs ρ for different origami structures). For each origami structure, since the triangular facet ratio is a key variable in the rigidity percolation study, we record the triangular facet ratio and its corresponding critical transition density under different selection rules and numbers of choices k. Detailed numerical data can be found in Supplementary Note 4.

In Fig. 8(a), we present a 3D plot of the critical transition density ρ^* against the selection parameter $(-1)^r \cdot \log(k)$, where $r = 1$ corresponds to the Most Efficient selection rule and $r = 2$ to the Least Efficient selection rule. We also include the triangular facet ratio t as a structural parameter in the 3D plot. Note that when $k = 1$, both rules reduce to fully stochastic selection since only one candidate is available. In this case, the selection parameter $(-1)^r \cdot \log(k)$ equals zero, and the critical transition density ρ^* corresponds to the average of the ρ^* values obtained under the two rules. See also

Supplementary Note 4 and Supplementary Movie 3 for additional results, accuracy estimation and visualizations.

From the 3D plot, we observe that for rotational origami structures, smaller resolutions tend to exhibit higher critical transition densities, as increasing the resolution changes the component ratio of the polygonal facet types. In contrast, resolution has little effect on periodic and perforated origami structures, since repeating the unit cell does not change the composition and the component ratio of the polygonal facets type. We conclude that if the change of pattern resolution does not significantly affect the facets ratio, then it does not significantly affect the critical transition density.

It is noteworthy that the underlying philosophies of the two rules are fundamentally reversed as k increases on both sides. At $k = 1$, both rules behave as fully stochastic selection strategies. As k increases from this baseline, the Most Efficient selection rule tends to favor selecting multi-vertex facets, while the Least Efficient selection rule increasingly avoids them. To highlight this contrast, data points from both rules are combined into a single plot, as shown in Fig. 8a.

Moreover, note that the more a facet is avoided under one rule, the more likely it is to be selected under the other. Avoiding certain types of facets is intuitively easier: if a facet does not appear in the k-candidate pool (especially when k is small), it is automatically avoided. Even if it appears, the rule can be used to steer selection away from it. Therefore, under the Least Efficient selection rule, both the rule itself and smaller values of k contribute to avoiding undesired facets. As a result, even small values of k can significantly delay the reduction of DOF, producing a similar effect as larger k.

In contrast, actively favoring a specific facet type is more difficult than simply avoiding it. It first requires the facet to appear in the k-candidate pool through stochastic sampling, and then be selected. Thus, to ensure consistent selection of desired facets, k must be sufficiently large to provide enough candidate options. Therefore, while k influences both rules, its effect is more sustained under the Most Efficient selection rule.

The duality and above contrast of two rules explain the rapid change in the critical transition density ρ^* within $k \in [-4, 8]$, with a symmetry center slightly biased toward the Most Efficient selection rule. Beyond this range, ρ^* remains relatively stable across all structures.

Recognizing the symmetric behavior in the simulation results, we observe that ρ^* varies significantly around a central value of k, with the center of symmetry slightly shifted to the right. More specifically, all curves appear to be centered around the right of the point $(-1)^r \cdot \log(k) = 0$, i.e., when $k = 1$, and origami structures with different triangular facet ratios t give different center values. Moreover, in general, the center value shows clearly different trends for different t. This suggests that ρ^* partially depends on a function of t. Additionally, for both the Most Efficient selection rule ($r = 1$) and the Least Efficient selection rule ($r = 2$), the simulated ρ^* values tend to stabilize as k increases. Hence, we fit the simulation results using a tanh-based model with parameters that control both the steepness and the center of symmetry. Specifically, we consider the following model:

$$\rho^*_{\text{fit}}(r, k, t) = a \cdot \tanh\left(b \cdot (-1)^r \cdot \log(k) + c\right) + dt + f, \qquad (21)$$

where k is the number of candidate facets, $r \in \{1, 2\}$ denotes the rule type, t is the triangular facet ratio, and a, b, c, d, f are fitting parameters. By fitting this model to each origami structure and resolution, we see that the fitted result ρ^*_{fit} matches the simulated values ρ^* both qualitatively and quantitatively (see Fig. 8b and the detailed results in Supplementary Note 4). Thus, for any given origami pattern and resolution, we can predict the critical transition density using the corresponding fitted parameters.

Moreover, the fitted parameters in Eq. (21) can provide us with meaningful insights into the physical properties of the origami patterns. Intuitively, a represents the magnitude of the difference between the effect of the Most Efficient and Least Efficient selection rules for the given origami pattern. Also, the parameter b reflects the sharpness of the change in the critical transition density as we move from one of the rules to the other, and the parameter c captures the asymmetry of the transition density change. Finally, the remaining two parameters d and f are relevant to some "intrinsic" properties of the structure regardless of our control. More specifically:

- a sets the saturation amplitude of the k-dependent effect. In particular, as $k \to \infty$, the two branches approach values that differ by approximately $2a$, so a quantifies the maximal separation between the two regimes.
- b controls the sensitivity to $\log(k)$, i.e., how quickly ρ^* transitions from one saturated regime to the other as k increases.
- c is a horizontal shift term in $\log(k)$, which determines the effective threshold k at which the transition occurs.
- d quantifies the average stage-to-stage drift of ρ^* as planarity constraints are progressively activated.
- f is a global offset capturing the k-independent baseline level set by the geometry/topology and the chosen normalization of ρ^*.

The critical transition in rigidity percolation marks the point at which an origami structure becomes mechanically rigid or significantly less flexible, and serves as a key design target for applications such as mechanical memory, tunable stiffness, and reconfigurable metamaterials. For high-resolution structures, direct simulation is computationally expensive. Instead, by computing the triangular facet ratio t of high-resolution origami structures, one can use the fitted model to predict the critical transition density $\rho^*_{\text{fit}}(r, k, t)$ for given values of r and k. One can also use the fitted model in a reversed way to achieve a desired critical transition density. Given a high-resolution origami structure with triangular facet ratio t, the model allows determining suitable values of the selection rule r and the number of choices k required to reach the target rigidity. In physical rigidity-based origami, if a desired number of rigidified facets is specified as $N_r = \rho^*_{\text{fit}}(r, k, t) \times (\text{total number of facets})$, one can select appropriate values of the selection rule r and the number of choices k accordingly. By referring to the recorded selection history from rigidity percolation simulations, these constraints can then be directly applied to the physical structure. This approach enables the physical construction of a significantly less flexible origami design that contains the desired number of rigidified facets.

Discussion

In this work, we have studied the rigidity control of various types of origami structures with different periodicity properties, rotational symmetries, and topologies. In particular, we have considered how different selection rules in changing the facet planarity will affect the rigidity and percolation transitions of different origami structures. We have shown that the changes in the degrees of freedom of periodic origami structures generally exhibit a combination of linear and nonlinear regimes similar to that of the well-known Miura-Ori structures. For rotational origami structures, the central facet plays an important role and can hence lead to a larger variation in the rigidity transition. By contrast, for perforated origami structures, the individual facet planarity conditions are less related to each other due to the cuts, and hence the DOF will generally decrease straightly under the Most Efficient selection rule, until only the "redundant" facets are left, and the trend under the Least Efficient selection rule will be the opposite.

More generally, one can see that in all origami structures, the rigidity control is highly relevant to the presence of triangular facets. Moreover, by analyzing the critical transition density ρ^*, one can observe the duality between the Most Efficient selection rule and the Least Efficient selection rule. The relationship between the number of choices k, the type of the selection rule r, the triangular facet ratio t, and the critical transition density ρ^* can be described by a simple model involving a hyperbolic tangent function and some other linear terms. Altogether, this paves a new way for the analysis of the rigidity control of general origami structures and other art-inspired mechanical metamaterials.

From a statistical viewpoint, starting with the hypergeometric model, we estimate the probability of DOF change at a given ρ and show that the triangular facet ratio is a key variable. A natural next step is to define

additional concepts and introduce necessary assumptions into the stochastic process of random sampling of k-candidates and selection. One can then study the expectation $\mathbb{E}[\rho^*]$, variance $\mathrm{Var}[\rho^*]$, where $\rho^* = \arg\min_\rho d(\rho) = d_{\mathrm{final}}$ and further model the simulation process using a stochastic differential equation framework. This provides more theoretical insights into the critical transition and its width. Also, as shown in prior studies of origami with quadrilateral facets[40–42], a proper design of the initial distribution of the creases may influence the rigidity. Therefore, one potential direction is to explore how crease design interacts with rigidity percolation under our rigidity control framework. Another natural next step is to extend our study to the rigidity control of curved fold origami structures[43–46] and other two- and three-dimensional structural assemblies[47–49]. For instance, the relationship between the number of DOFs and the number of revolute joints in ori-kiri assemblages has been recently studied[50], and one possible future direction is to incorporate the type of joints into our rigidity control formulation.

Data availability

All relevant data files are available on Zenodo at https://doi.org/10.5281/zenodo.16617901.

Code availability

Simulation codes are available on Zenodo at https://doi.org/10.5281/zenodo.16617901.

Received: 18 August 2025; Accepted: 10 April 2026;
Published online: 25 April 2026

References

1. Hatori, K. History of origami in the east and the west before interfusion. *Origami 5: Fifth Int. Meet. Origami Sci., Math., Educ.* **5**, 1–10 (2011).
2. Huffman Curvature and creases: A primer on paper. *IEEE Trans. Comput.* **100**, 1010–1019 (1976).
3. Hull, T. On the mathematics of flat origamis. Congr. Numer.215-224 (1994).
4. Lang, R. J. A computational algorithm for origami design. In *Proceedings of the Twelfth Annual Symposium on Computational Geometry*, 98-105 (1996).
5. Kawasaki, T.Roses, origami & math (Japan Publications Trading, 2005).
6. Demaine, E. D. & O'Rourke, J.Geometric folding algorithms: linkages, origami, polyhedra (Cambridge University Press, 2007).
7. Tachi, T. Origamizing polyhedral surfaces. *IEEE Trans. Vis. Comput. Graph.* **16**, 298–311 (2009).
8. Lang, R. J.Origami design secrets: mathematical methods for an ancient art (CRC Press, 2012).
9. Rus, D. & Tolley, M. T. Design, fabrication and control of origami robots. *Nat. Rev. Mater.* **3**, 101–112 (2018).
10. Ze, Q. et al. Soft robotic origami crawler. *Sci. Adv.* **8**, eabm7834 (2022).
11. Treml, B., Gillman, A., Buskohl, P. & Vaia, R. Origami mechanologic. *Proc. Natl. Acad. Sci.* **115**, 6916–6921 (2018).
12. Meng, Z. et al. Bistability-based foldable origami mechanical logic gates. *Extrem. Mech. Lett.* **43**, 101180 (2021).
13. Nishiyama, Y. Miura folding: Applying origami to space exploration. *Int. J. Pure Appl. Math.* **79**, 269–279 (2012).
14. Miura, K. Method of packaging and deployment of large membranes in space. The Institute of Space and Astronautical Science Report1-9 (1985).
15. Wei, Z. Y., Guo, Z. V., Dudte, L., Liang, H. Y. & Mahadevan, L. Geometric mechanics of periodic pleated origami. *Phy. Rev. Lett.* **110**, 215501 (2013).
16. Schenk, M. & Guest, S. D. Geometry of Miura-folded metamaterials. *Proc. Natl. Acad. Sci.* **110**, 3276–3281 (2013).
17. Dudte, L. H., Vouga, E., Tachi, T. & Mahadevan, L. Programming curvature using origami tessellations. *Nat. Mater.* **15**, 583–588 (2016).
18. Dudte, L. H., Choi, G. P. T. & Mahadevan, L. An additive algorithm for origami design. *Proc. Natl. Acad. Sci.* **118**, e2019241118 (2021).
19. Chen, S. & Mahadevan, L. Rigidity percolation and geometric information in floppy origami. *Proc. Natl. Acad. Sci.* **116**, 8119–8124 (2019).
20. Li, R. & Choi, G. P. T. Explosive rigidity percolation in origami. *Proc. R. Soc. A* **481**, 20240826 (2025).
21. Achlioptas, D., D'Souza, R. M. & Spencer, J. Explosive percolation in random networks. *Science* **323**, 1453–1455 (2009).
22. Araujo, N. A. M. & Herrmann, H. J. Explosive percolation via control of the largest cluster. *Phys. Rev. Lett.* **105**, 035701 (2010).
23. Riordan, O. & Warnke, L. Explosive percolation is continuous. *Science* **333**, 322–324 (2011).
24. Chen, B. G. -g & Santangelo, C. D. Branches of triangulated origami near the unfolded state. *Phys. Rev. X* **8**, 011034 (2018).
25. He, Z. & Guest, S. D. On rigid origami I: piecewise-planar paper with straight-line creases. *Proc. R. Soc. A* **475**, 20190215 (2019).
26. He, Z. & Guest, S. D. On rigid origami II: quadrilateral creased papers. *Proc. R. Soc. A* **476**, 20200020 (2020).
27. He, Z. & Guest, S. D. On rigid origami III: local rigidity analysis. *Proc. R. Soc. A* **478**, 20210589 (2022).
28. Zhang, H. et al. Rigidity analysis and mechanical properties of programmable origami tubes. *Mech. Res. Commun.* **132**, 104182 (2023).
29. Davis, E., Demaine, E. D., Demaine, M. L. & Ramseyer, J. Reconstructing david huffman's origami tessellations. *J. Mech. Des.* **135**, 111010 (2013).
30. Origami Simulator. https://origamisimulator.org/ (2018).
31. Ghassaei, A., Demaine, E. D. & Gershenfeld, N. Fast, interactive origami simulation using GPU computation. In *Origami7: Proceedings of the 7th International Meeting on Origami in Science, Mathematics and Education (OSME 2018)*, vol. 7, 1151–1166 (2018).
32. Scheffer, M. et al. Early-warning signals for critical transitions. *Nature* **461**, 53–59 (2009).
33. Scheffer, M. et al. Anticipating critical transitions. *Science* **338**, 344–348 (2012).
34. Kong, L.-W., Fan, H.-W., Grebogi, C. & Lai, Y.-C. Machine learning prediction of critical transition and system collapse. *Phys. Rev. Res.* **3**, 013090 (2021).
35. Han, H., Sorokin, V., Tang, L. & Cao, D. Origami-based tunable mechanical memory metamaterial for vibration attenuation. *Mech. Syst. Signal Process.* **188**, 110033 (2023).
36. Zang, S., Misseroni, D., Zhao, T. & Paulino, G. H. Kresling origami mechanics explained: Experiments and theory. *J. Mech. Phys. Solids* **188**, 105630 (2024).
37. Guest, S. The stiffness of prestressed frameworks: a unifying approach. *Int. J. Solids Struct.* **43**, 842–854 (2006).
38. Radicchi, F. & Fortunato, S. Explosive percolation in scale-free networks. *Phys. Rev. Lett.* **103**, 168701 (2009).
39. Chen, S., Choi, G. P. T. & Mahadevan, L. Deterministic and stochastic control of kirigami topology. *Proc. Natl. Acad. Sci.* **117**, 4511–4517 (2020).
40. Izmestiev, I. Classification of flexible Kokotsakis polyhedra with quadrangular base. *Int. Math. Res. Not.* **2017**, 715–808 (2017).
41. Lang, R. J. & Howell, L. Rigidly foldable quadrilateral meshes from angle arrays. *J. Mech. Robot.* **10**, 021004 (2018).
42. Feng, F., Dang, X., James, R. D. & Plucinsky, P. The designs and deformations of rigidly and flat-foldable quadrilateral mesh origami. *J. Mech. Phys. Solids* **142**, 104018 (2020).
43. Dias, M. A. & Santangelo, C. D. The shape and mechanics of curved-fold origami structures. *Europhys. Lett.* **100**, 54005 (2012).
44. Liu, H. & James, R. D. Design of origami structures with curved tiles between the creases. *J. Mech. Phys. Solids* **185**, 105559 (2024).
45. Chai, S., Hu, Z., Chen, Y., You, Z. & Ma, J. Programmable multi-stability of curved-crease origami structures with travelling folds. *J. Mech. Phys. Solids* **193**, 105877 (2024).

46. Song, K., Li, H., Li, Y., Ma, J. & Zhou, X. A review of curved crease origami: design, analysis, and applications. *Front. Phys.* **12**, 1393435 (2024).
47. Lubbers, L. A. & van Hecke, M. Excess floppy modes and multibranched mechanisms in metamaterials with symmetries. *Phys. Rev. E* **100**, 021001 (2019).
48. Overvelde, J. T. B., Weaver, J. C., Hoberman, C. & Bertoldi, K. Rational design of reconfigurable prismatic architected materials. *Nature* **541**, 347–352 (2017).
49. Choi, G. P. T., Chen, S. & Mahadevan, L. Control of connectivity and rigidity in prismatic assemblies. *Proc. R. Soc. A* **476**, 20200485 (2020).
50. Dang, X., Chen, S., Acha, A. E., Wu, L. & Pasini, D. Shape and topology morphing of closed surfaces integrating origami and kirigami. *Sci. Adv.* **11**, eads5659 (2025).

Acknowledgements

This work was supported in part by the CUHK Faculty of Science Direct Grant for Research, grant no. 4053710 (to G.P.T.C.).

Author contributions

G.P.T.C. conceived the research. R.L. and G.P.T.C. designed the research, implemented the algorithms, conducted the numerical experiments, analyzed the results, and wrote the manuscript.

Competing interests

The authors declare no competing interests.

Additional information

Supplementary information The online version contains supplementary material available at https://doi.org/10.1038/s42005-026-02640-5.

Correspondence and requests for materials should be addressed to Gary P. T. Choi.

Peer review information : *Communications Physics* thanks the anonymous reviewers for their contribution to the peer review of this work.